



Numerical and experimental investigation of flame dynamics in opposed-flow solid fuel burner

Ryan DeBoskey^{a,b}, Clayton Geipel^c, David Kessler^d, Brian Bojko^d, Brian Fisher^c,
Ryan F. Johnson^d, Venkat Narayanaswamy^a

^a North Carolina State University, Department of Mechanical and Aerospace Engineering, Raleigh, 27695, NC, USA

^b Commonwealth Technology Innovation LLC, A Huntington Ingalls Industries Company, Alexandria, 22315, VA, USA

^c Chemistry Division, Combustion and Reacting Transport Section, Code 6185, Naval Research Laboratory, WA, 20375, DC, USA

^d Laboratories for Computational Physics and Fluid Dynamics, Code 6041, Naval Research Laboratory, WA, 20170, DC, USA

ARTICLE INFO

Keywords:

Solid fuel

Opposed-flow burner

Flame thickness

Large-eddy simulation

ABSTRACT

Understanding the complex coupled physics of phase change and turbulent gas-phase combustion in solid fuel combustors is critical to the design of advanced propulsion systems. This study considers the combustion of hydroxyl-terminated polybutadiene (HTPB) in an opposed-flow burner (OFB) configuration. High-speed shadowgraph imaging on the OFB is conducted to capture the unsteady flame dynamics surrounding the burner. Unsteady two-dimensional axisymmetric simulations, performed using a high-fidelity 20-species, 109-reaction pressure comprehensive skeletal kinetics mechanism, show improved agreement in the prediction of flame thickness in comparison to previous quasi-one-dimensional modeling, attributed to the significant deviation from self-similarity in the OFB configuration. Experimental and numerical data are compared showing strong trend-wise agreement and providing novel insight into the hitherto unexplored complex dynamics of the OFB configuration. Power spectral density (PSD) profiles of the flame oscillations demonstrate strong agreement in the broad peak frequency between simulations and experiments. PSD of flame thickness, regression rate, and azimuthal vorticity from the computed flame dynamics show strong coupling between the instantaneous regression rate and flame thickness, which is largely driven by the low-frequency vortex shedding from the OFB nozzle lip. Snapshots of the flowfield show a secondary diffusion flame with the majority of CO to CO₂ oxidation downstream of the fuel grain edge. Variations in the species composition along the fuel surface highlight the complex balance between convective and diffusive forces arising from the proximity of the stagnation plane adjacent to the fuel surface.

Novelty and Significance Statement

This work utilizes large-eddy simulation (LES) to improve the prediction of flame thickness by 1000+% in an opposed flow solid fuel burner (OFB). Demonstration of significant deviation from self-similarity profiles highlight the limitations of current state-of-the-art quasi one-dimensional modeling techniques and provides a viable strategy for predictive modeling of solid fuel combustion systems. Accurate prediction of heterogeneous combustion is a critical challenge limiting propellant and fuel discovery. Alongside validating experimental data, high-fidelity numerical simulations of heterogeneous combustion systems are of topical importance to advancing community understanding. High-fidelity modeling and experimental imaging gives unprecedented insight into the coupling between solid fuel combustion, unsteady flame dynamics, and unsteady fluid dynamics.

1. Introduction

Hydroxyl-terminated polybutadiene (HTPB) has been extensively studied due to its prevalent use as a propellant binder in solid-rocket motors [1]. HTPB has recently gained renewed interest in its role as the

primary fuel in hybrid rocket engines (HRE), solid fuel ramjet (SFRJ), and solid fuel scramjet engines [2–5]. HTPB traditionally serves both as a fuel and a binder, serving as a polymer matrix to hold together an oxidizer component, commonly ammonium perchlorate (AP), with

* Corresponding author at: North Carolina State University, Department of Mechanical and Aerospace Engineering, Raleigh, 27695, NC, USA.

E-mail address: rddebosk@ncsu.edu (R. DeBoskey).

¹ National Defense Science and Engineering Graduate (NDSEG) Fellow.

energetic fuels such as solid particles. There is a vast array of literature on HTPB/AP combustion and the role of HTPB in solid-rocket motor applications [6], but the utilization of HTPB as a primary fuel and in environments different from typical solid-rocket motors necessitates further investigation.

Several experimental studies have been performed to characterize the performance of solid fuels, typically for regression rates in engine-specific applications [7]. These studies provide valuable data on the average regression and performance of HTPB fuel, but in-situ measurements reveal a high degree of variations, often containing scale and geometry dependencies. The opposed-flow burner (OFB) configuration overcomes these issues by simply impinging an oxidizer jet on the solid fuel surface and establishing a diffusion flame. First introduced by Blazowski [8], the simplified geometry reduces the dimensionality and focuses on the coupled combustion and pyrolysis process. The OFB configuration has been used to characterize various solid fuels; providing burn rates, extinction limits, species profiles, and temperature profiles [8–18]. Notably, several studies have utilized the OFB configuration and neat HTPB to determine the effect of oxidizer composition, the addition of metal particles, and alternative fuels on regression rate, flame structure, and flame temperature [11,16–18]. Power-law fits of the regression rate across pressure, oxidizer composition, and oxidizer mass flux from the OFB have been commonly used for practical engine design. Recent work has demonstrated the utility of regression models derived from OFB experiments to simulate the combustion physics within solid fuel ramjets in unsteady simulations [19,20].

Accompanying numerical simulations of the OFB configuration have been performed to better understand the fundamental heterogeneous combustion phenomenon and develop towards predictive models. Early work by Krishnamurthy et al. [21] described an analytical solution to the stagnation-point boundary-layer flow of a condensed fuel. Extensions of this analysis led to closed algebraic forms, extinction strain rate prediction, and inclusion of radiation effects for solid fuel flames [10, 22,23]. Using simplified transport models and a one-step chemistry model, this work simulated the basic flame structure in good agreement with experimental observations providing parametric and theoretical insight. Later, Risha et al. [11] demonstrated prediction of regression rate within 10% using a semi-empirical fit derived from Marxman's analysis [24]. Although insightful, these calculations remained largely non-predictive due to large uncertainties in gas-phase combustion kinetics and transport properties, requiring parametric fits. Using self-similar counterflow calculations with modified boundary conditions, Pace et al. [20] found good agreement with experimental PMMA flame standoff and regression rate at low mass flux. Previous work by authors has demonstrated strong trend-wise agreement between the results of quasi-one-dimensional simulations with detailed kinetics and experimental data [18] describing the fuel regression rate and gas-phase flame thickness with HTPB; however, the magnitudes of the simulated flame thicknesses were substantially different from the experimental values considered at higher mass flux.

The OFB configuration differs considerably from the canonical counterflow configuration, questioning the validity of the quasi-one-dimensional assumption. Extensive studies have explored the influence of geometry in meeting the essential assumptions required to apply quasi-one-dimensional stagnation flow theory in opposed flow burners, both experimentally [25–28] and numerically [29–32]. The results of these works underscore the importance of accounting for nozzle geometry when seeking to compare with quasi-one-dimensional theory. These prior works demonstrated conclusively that extensive care must be used in order to utilize quasi-one-dimensional theory to properly apply academically counterflow solvers [33–35] to meet self-similarity requirements for real experimental flames. In the OFB configuration, the oxidizer flow rate is several orders of magnitude higher than the fuel blowing velocity from pyrolysis, resulting in a stagnation point that is very close to the solid fuel boundary. Radial discrepancy in the solid fuel surface regression rate and composition are a hitherto unexplored

aspect of the OFB configuration, resulting in a non-uniform fuel inflow boundary due to the competition between convective and diffusive fluxes near the surface. Consequently, this questions the validity of meeting the self-similarity requirements at the solid fuel surface and potentially prohibits the utilization of quasi-one-dimensional theory for accurate assessment of OFB flame dynamics.

Steady quasi-one-dimensional flames and algebraic forms are further unable to capture the unsteady dynamics and the rich physics in the outer regions of the OFB configuration. Indications of higher-dimensional effects surfaced in the first OFB experiments performed by Shark et al. [16], in which the onset of turbulence resulted in different regression rate trends as compared to the laminar flow regime. These unsteady and higher-dimensional effects offer a potential to study the coupled unsteady fuel pyrolysis, gas-phase combustion, and fluid dynamics in a canonical, unobstructed, and accessible geometry. Flame dynamics along and downstream of the fuel surface are subject to high convective strain, similar to large-scale propulsive engines. This allows for quick and efficient testing of numerical solvers for heterogeneous combustion, vital to improving large-scale modeling of HRE and SFRJ engines, with readily available experimental validation.

This work temporally simulates the OFB combustor using two-dimensional axisymmetric large-eddy simulations (LES) in order to explore the coupled unsteady flow dynamics, flame structure, and fuel regression. The rest of the paper is organized as follows. First, the experimental OFB setup is introduced with details on shadowgraph imaging data collection. Next, the numerical methodology is introduced describing the model geometry and problem, the kinetics model, and the gas-phase simulation method. Comparisons between the experimental and numerical flame thickness and surface regression are presented to explore the spatial and temporal variance in flame structure. Lastly, final conclusions are drawn and future work is described.

2. Experimental setup

HTPB fuel strands employed for the experimental tests had a nominal diameter of 16 mm and a nominal length of 25 mm. HTPB resin (R-45M, CRS Chemicals) was first mixed with a curative (isophorone diisocyanate, 10 wt%, Thermo Scientific Chemicals, purity >98%) and a cure catalyst (triphenylbismuth, 0.2 wt%, Thermo Scientific Chemicals, purity >98%) for ten minutes under vacuum. The mixture was then poured into cylindrical molds and cured at 60–70 °C for 72 h. The strands were then cut to length and stored in a desiccator at ambient temperature and pressure and 15% relative humidity until burn testing.

Experimental measurements were performed at the Naval Research Laboratory OFB facility. A schematic of this burner is shown in Fig. 1. The fuel strand of nominal diameter 16 mm was secured within a fuel holder, which comprised of an aluminum tube of inner diameter 16.25 mm. The strand was positioned by a stepper motor and protruded above the top of the fuel holder by about 2 mm. A contoured oxidizer nozzle with exit diameter 7.25 mm and lip thickness of 1.59 mm was directed at the fuel surface, separated from the fuel surface by $\Delta z = 10$ mm. A diode laser beam with a 3 mm \times 5 mm elliptical cross section was collected by a photodiode through a bandpass filter, which was used to dynamically maintain the fuel surface at the same vertical location by compensating for the fuel regression. An electric match was placed on the strand surface to ignite the fuel surface.

Prior to fuel ignition, a mass flow controller was used to produce a stream of oxygen with an average mass flux 26 kg/(m²s) that impinged on the fuel surface. Upon ignition, the photodiode signal was compared to a target signal level and the error is used in a proportional–integral control loop to command the stepper motor to maintain a constant position of the burning surface. The movement of the motor was recorded at 4 Hz and used to compute the bulk regression rate. At the conclusion of the test, the oxygen stream was replaced with a nitrogen stream to extinguish the flame. A complete description of the burner and testing procedure has been published previously [36].

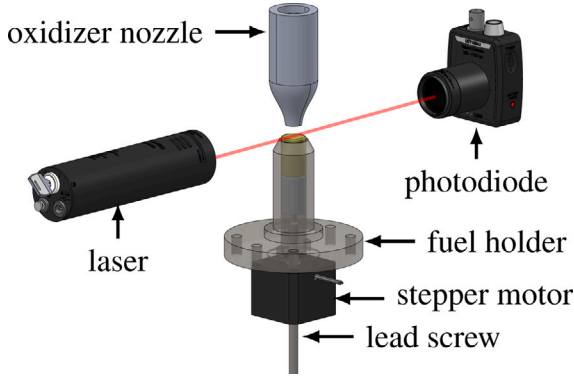


Fig. 1. Naval Research Laboratory opposed-flow burner.

High-speed shadowgraph imaging was used to measure flame thickness during strand combustion. The light from an LED source (ISSI, LZ-620, central wavelength 633 nm) passed through a ground-glass diffuser and was then collimated by a plano-convex lens ($f = 150$ mm, diameter 50 mm). The lightfield transited the flame and was imaged by a high-speed camera (Photron, Fastcam SA5) through a bandpass filter (Andover, 633FSX10-50), an objective ($f = 200$ mm, $f/2.8$), and an extension tube of length 200 mm. Images were collected at 42 kHz with an exposure time of 10 μ s. Images had 512 pixels in the radial direction r and 320 pixels in the axial direction z , spanning r from 0.37 to 8.18 mm and z from -2.64 to 2.23 mm, where the coordinate system originated in the center of the burning strand surface. A set of 1000 images of the experiment was processed. These images spanned 23.81 ms with a repetition rate of 42 kHz.

3. Numerical method

3.1. Governing equations

Inside the fluid domain, we solve the compressible, multicomponent, chemically reacting Navier–Stokes equations, given generally by:

$$\frac{\partial y}{\partial t} + \nabla \cdot F(y, \nabla y) - S(y) = 0 \quad (1)$$

where y is the state vector, ∇y is its spatial gradient, t is time, F is the flux, and $S = (0, \dots, 0, 0, \omega_1, \dots, \omega_{n_s})^T$ is the chemical source term, with ω_i corresponding to the net chemical production rate of the i th species. The physical coordinates are denoted by $x = (x_1, \dots, x_d)$, with d spatial dimensions. The vector of state variables is expanded as:

$$y = (\rho v_1, \dots, \rho v_d, \rho e_t, C_1, \dots, C_{n_s})^T \quad (2)$$

where ρ is density, $v = (v_1, \dots, v_d)$ is the velocity vector, e_t is the specific total energy, $C = (C_1, \dots, C_{n_s})$ is the vector of molar concentrations, and n_s is the number of species. The partial density of the i th species is defined as:

$$\rho_i = W_i C_i \quad (3)$$

where W_i is the molecular weight of the i th species, from which the density can be computed as:

$$\rho = \sum_{i=1}^{n_s} \rho_i \quad (4)$$

The mole and mass fractions of the i th species, X_i and Y_i , respectively, are given by:

$$X_i = \frac{C_i}{\sum_{i=1}^{n_s} C_i}, \quad Y_i = \frac{\rho_i}{\rho}. \quad (5)$$

The equation of state for the mixture is written as:

$$P = R^0 T \sum_{i=1}^{n_s} C_i, \quad (6)$$

where P is the pressure, T is the temperature, and R^0 is the universal gas constant. The specific total energy is the sum of the mixture-averaged specific internal energy, u , and the specific kinetic energy, written as:

$$e_t = u + \frac{1}{2} \sum_{k=1}^d v_k v_k \quad (7)$$

where the former is the mass-weighted sum of the specific internal energies of each species, given by:

$$u = \sum_{i=1}^{n_s} Y_i u_i \quad (8)$$

With the thermally perfect gas model, u_i is defined as:

$$u_i = h_i - R_i T = h_{\text{ref},i} + \int_{T_{\text{ref}}}^T c_{p,i}(\tau) d\tau - R_i T \quad (9)$$

where h_i is the specific enthalpy of the i th species, $R_i = R^0/W_i$, T_{ref} is the reference temperature of 298.15 K, $h_{\text{ref},i}$ is the reference-state species formation enthalpy, and $c_{p,i}$ is the specific heat at constant pressure of the i th species, which is approximated with a polynomial as a function of temperature based on the NASA coefficients [37,38]:

$$c_{p,i} = \sum_{k=0}^{n_p} a_{ik} T^k. \quad (10)$$

The flux can be expressed as the difference between the convective flux, F^c , and the viscous flux, F^v :

$$F(y, \nabla y) = (F^c(y) - F^v(y, \nabla y)), \quad (11)$$

where the k th spatial components are defined as:

$$F_k^c(y) = (\rho v_k v_1 + P \delta_{k1}, \dots, \rho v_k v_d + P \delta_{kd}, v_k (\rho e_t + P), v_k C_1, \dots, v_k C_{n_s})^T \quad (12)$$

$$F_k^v(y, \nabla y) = \left(\tau_{1k}, \dots, \tau_{dk}, \sum_{j=1}^d \tau_{kj} v_j + \sum_{i=1}^{n_s} W_i C_i h_i V_{ik} - q_k, C_1 V_{1k}, \dots, C_{n_s} V_{n_s k} \right)^T \quad (13)$$

where τ is the viscous stress tensor, q is the heat flux, and V_{ik} is the k th spatial component of the diffusion velocity of the i th species, defined as:

$$V_{ik} = \hat{V}_{ik} - \frac{\sum_{l=1}^{n_s} W_l C_l \hat{V}_{lk}}{\rho}, \quad \hat{V}_{ik} = \frac{\bar{D}_i}{C_i} \frac{\partial C_i}{\partial x_k} - \frac{\bar{D}_i}{\rho} \frac{\partial \rho}{\partial x_k}, \quad (14)$$

which includes a standard correction to ensure mass conservation (i.e., $\sum_{i=1}^{n_s} W_i C_i V_{ik} = 0$) [39,40]. \bar{D}_i is the mixture-averaged diffusion coefficient of the i th species, obtained as: [41]

$$\bar{D}_i = \frac{1}{\bar{W}} \frac{\sum_{j=1, j \neq i}^{n_s} X_j W_j}{\sum_{j=1, j \neq i}^{n_s} X_j / D_{ij}}, \quad (15)$$

where $P_{\text{atm}} = 1$ atm, $\bar{W} = \rho / \sum_i C_i$ is the mixture molecular weight, and D_{ij} is the binary diffusion coefficient between the i th and j th species, which is a positive function of temperature and pressure [35,42]. Note that \bar{D}_i can be nonzero for $C_i = 0$. The k th spatial components of the viscous stress tensor and the heat flux are written as:

$$\tau_k(y, \nabla y) = \mu \left(\frac{\partial v_1}{\partial x_k} + \frac{\partial v_k}{\partial x_1} - \delta_{k1} \frac{2}{3} \sum_{j=1}^d \frac{\partial v_j}{\partial x_j}, \dots, \frac{\partial v_d}{\partial x_k} + \frac{\partial v_k}{\partial x_d} - \delta_{kd} \frac{2}{3} \sum_{j=1}^d \frac{\partial v_j}{\partial x_j} \right) \quad (16)$$

where μ is the dynamic viscosity, calculated using the Wilke model [43], and:

$$q_k(y, \nabla y) = -\lambda_T \frac{\partial T}{\partial x_k} \quad (17)$$

where λ_T is the thermal conductivity, computed with the Mathur model [44], respectively.

Eq. (1)–(13) were solved using an extended version of the JENRE[®] Multiphysics Framework. The underlying flow solver utilizes a nodal discontinuous Galerkin (DG) finite-element formulation, with linear DG ($p = 1$) basis functions. The flow solver uses an implicit LES formulation that provides numerical dissipation. The HLLC approximate Riemann solver was used to compute the numerical flux across adjacent element faces, and the Bassi–Rebay (BR2) method [45] is used to discretize the viscous fluxes. Time integration was done explicitly using a 11-stage 2nd-order strong stability-preserving Runge–Kutta method [46]. For the finite-rate kinetics simulations, reaction source terms were applied using a Strang-splitting approach, in which the system of stiff chemical reaction rate laws were integrated implicitly using the DGODE method as described by Johnson and Kercher [47]. Spatial discretization error of the reacting solver has been verified to converge with the expected optimal ($p + 1$) rate [47]. The axisymmetric formulation of the flow solver is based on that described by Bassi et al. [48].

3.2. Solid fuel pyrolysis model

For the interfacial solid–gas coupling, we utilized a simplified model for the pyrolysis of the solid fuel grain as described in a previous work [49], which assumes thermal equilibrium at the surface. This assumption eliminates the need to solve for the energy transport in the solid fuel material, and the material interface condition reduces to a boundary condition for the gas-phase flow which sets the temperature, density, and species mass fractions at the solid fuel grain according to the following set of conservation equations:

$$\frac{\dot{m}_s''}{W_s} = \left[C_s v - D_{sg} \left(\frac{\partial C_s}{\partial n} - \frac{C_s}{\rho} \frac{\partial \rho}{\partial n} \right) \right]_f \quad (18)$$

$$0 = \left[C_i v - D_i \left(\frac{\partial C_i}{\partial n} - \frac{C_i}{\rho} \frac{\partial \rho}{\partial n} \right) \right]_f \quad (19)$$

$$\dot{m}_s'' L = k_f \left(\frac{\partial T}{\partial n} \right)_f \quad (20)$$

where the subscripts ‘s’ and ‘i’ refer to the gas-phase pyrolysis product species and the other non-participating species, respectively. The right-hand side represents the gas-phase fluid, denoted by subscript ‘f’, and the left-hand side represents the solid-phase. Derivatives were computed in the direction ‘n’ normal to the interface, and L is the temperature-dependent latent heat of vaporization of the solid species. The surface blowing velocity is $v = \dot{m}_s'' / \rho$, where ρ is the density of the gas in the pyrolysis zone. The mass flux of the pyrolysis product was computed using a simplified model in which solid fuel was converted to a gaseous fuel species according to an Arrhenius law,

$$\dot{m}_s'' = \rho_s l_r A_p e^{-E_p / RT_I}, \quad (21)$$

where \dot{m}_s'' is the mass flux of fuel into the fluid region, l_r is the reaction thickness of the pyrolysis zone, and T_I is the temperature at the fluid–solid interface. We consider a solid fuel composed entirely of an idealized polymer with properties similar to hydroxyl-terminated polybutadiene (HTPB) that is fully converted to the gaseous hydrocarbon butadiene (C_4H_6). The thermophysical properties and the Arrhenius pyrolysis parameters used for the model HTPB are from Arisawa and Brill [50,51], and are given in Tables 1 and 2, respectively, which have been successfully used in past numerical simulations [52]. The enthalpy of the solid fuel material is related to temperature via an equation of state, $h_s = C_p T_I + e_0$, where C_p is the specific heat of the material and e_0 is a reference energy that enforces consistency with the gas-phase equation of state for the corresponding vapor species. The temperature-dependent latent heat is then defined as the difference between the solid phase and gas-phase enthalpies, $L = h_s - h_g$. Eqs. (18)–(21) then define a set of $n+1$ nonlinear equations for the concentrations of the n gas-phase species in the model and the interface temperature, which are solved using an iterative Gauss–Newton

Table 1
Thermophysical properties of model HTPB [50,51].

Density	Specific heat	Thermal conductivity
900 kg/m ³	1100 J/kg K	0.235 W/m K

Table 2
HTPB Arrhenius pyrolysis rate parameters [50,51].

A_p	E_p	l_r
$4.0889 \times 10^4 \text{ s}^{-1}$	$5.65 \times 10^7 \text{ J/kmol}$	$6 \times 10^{-5} \text{ m}$

Table 3
Model Problem Description.

Y_{O_2}	$\dot{m}_{ox}'' [\text{kg}/(\text{m}^2 \text{ s})]$	$\Delta z [\text{mm}]$	$P [\text{atm}]$	$T_{ox} [\text{K}]$
1.0	26	10	1	300

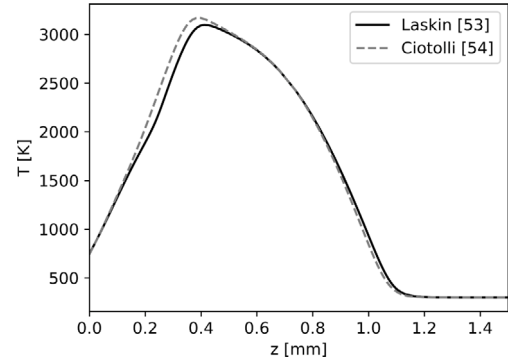


Fig. 2. Temperature profile comparison of chemical kinetics mechanisms in 1D solid fuel counterflow flame.

method.

3.3. Model problem

Numerical simulations were performed to assess the unsteady and two-dimensional flame dynamics of the OFB. All simulations considered the same model problem summarized in Table 3. The oxidizer inflow was pure oxygen at a nominal mass flux of 26 kg/(m² s) at standard conditions, with a separation distance Δz between the nozzle exit and the fuel surface of 10 mm.

First, quasi-one-dimensional flames were simulated in CANTERA using the Counterflow Diffusion Flame (CDF) solver [35] to assess the influence of the chemical kinetics mechanism on the flame characteristics and to provide a baseline of comparison for higher dimensional simulations. A fully coupled solid fuel boundary condition was used to define the fuel mass flux, pyrolysis gases, and surface temperature of the HTPB grain. The detailed formulation of the solid fuel boundary condition and thermophysical properties are given in previous work [18]. A detailed 94-species, 614-reaction, high-temperature kinetics mechanism developed by Laskin et al. [53] and a 20-species, 109-reaction, pressure-comprehensive skeletal kinetics model developed for hybrid rocket applications by Ciotolli et al. [54] were used to describe the gas-phase combustion of 1,3-butadiene (C_4H_6). Ciotolli et al. validated the 20-species skeletal mechanism against a detailed mechanism [55] for a series of 1,3-butadiene laminar counterflow flames. Comparison of the 20-species skeletal mechanism against the detailed mechanism is performed in this work to evaluate the performance of the skeletal mechanism with a coupled solid–gas interfacial boundary condition.

Fig. 2 shows the temperature profiles obtained using the 1D solid fuel counterflow solver with both chemical mechanisms. The results

Table 4

Summary comparison of chemical kinetics mechanisms in 1D solid fuel counterflow flame.

Mechanism	\dot{z} [mm/s]	T_s [K]	$Y_{C_4H_6,s}$	ℓ [mm]
Laskin [53]	0.377	741	0.74	1.044
Ciotolli [54]	0.394	748	0.76	1.030

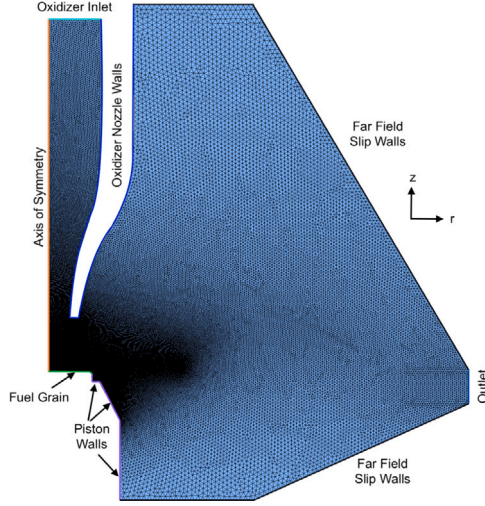


Fig. 3. Mesh of numerical axisymmetric OFB model. The fuel grain was modeled with a 1-mm rounded edge consistent with the rounding effect seen in experiments. The piston walls which held the solid fuel grains were modeled as isothermal walls at 750 K. The internal oxidizer nozzle walls were modeled using a slip wall, while the outer oxidizer nozzle walls are modeled as isothermal walls at 300 K. A subsonic outlet was used to maintain pressure within the domain.

show excellent agreement in flame structure, with the skeletal mechanism slightly overpredicting the peak flame temperature with the skeletal mechanism. Table 4 shows the summary of predicted regression rate, \dot{z} , surface temperature T_s , surface C_4H_6 mass fraction, $Y_{C_4H_6,s}$, and flame thickness, ℓ , between the two chemical mechanisms. The skeletal mechanism slightly overpredicts the fuel surface temperature (0.9%) and regression rate (4.5%), which is attributed to the slight overprediction of peak temperature. Although the regression rate predicted by the skeletal mechanism is higher, the flame thickness is slightly underpredicted in comparison to the detailed mechanism (1.3%). Having demonstrated sufficient physical accuracy in predicting the multiphase solid–gas coupling in comparison to the detailed mechanism, the skeletal mechanism by Ciotolli et al. [54] is used to solve the gas-phase chemistry in all further calculations.

Two-dimensional axisymmetric LES simulations of the OFB were performed to address the limitations of quasi-one-dimensional modeling. The coordinate system had radial coordinate r and axial coordinate z , originating at the center of the burning surface of the fuel grain. Fig. 3 shows the 2D mesh of the OFB computational domain with boundary conditions colored and labeled. Conditions at the oxidizer inlet were set to reproduce the mass flux used in experiments: 26 kg/(m² s) at the exit of the nozzle, with final simulations producing an average of 25.6 kg/(m² s). Two different boundary conditions, “Constant Inflow” and “Pyrolysis”, were considered at the fuel grain surface to decouple and study the influence of pyrolysis on flame dynamics. First, a constant inflow of C_4H_6 was blown in from the fuel grain boundary with a mass influx of 0.345 kg/(m² s) and temperature of 748 K, matching the quasi-one-dimensional solid fuel counterflow flame solution. Second, the fully coupled gas–solid interfacial boundary condition, Eqs. (18)–(20), was used to model the pyrolysis at the fuel grain surface.

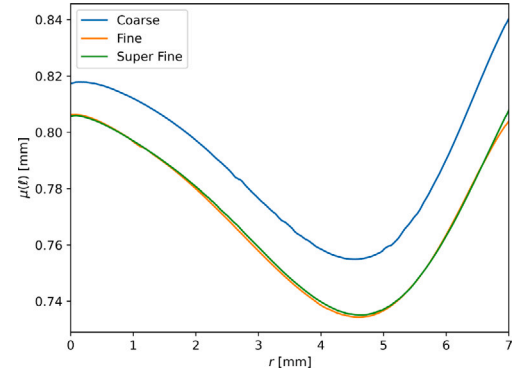


Fig. 4. Predicted average flame thickness with increasing grid resolution.

3.4. Grid independence study

A grid independence study was performed to ensure adequate resolution of the numerical solution. A coarse, fine, and super fine mesh were considered with minimum grid resolutions of 45 μm, 37.5 μm, and 33.5 μm, respectively, at the fuel grain surface. The resulting meshes contained 216k, 306k, and 380k elements, respectively. The study is performed using the constant inflow boundary condition to conserve computational cost. The numerical solution is sampled until convergence of the mean flame thickness profile, $\mu(\ell)$, to be defined in the succeeding section. Fig. 4 shows the results of the grid independence study, showing the predicted average flame thickness along the radius of the fuel grain with increasing grid resolution. There is good agreement between the magnitude and profile predicted between all numerical solutions, with error in magnitude of roughly 2% between the coarse and fine mesh. The coarse mesh predicts a slightly higher magnitude as a result of artificial flame stretching due to inadequate resolution. The profiles of the fine and super fine meshes coincide, indicating that the fine grid is sufficiently refined to accurately predict the flame thickness. Final simulations are performed on the fine mesh and sampled for a total of 5 ms at 120 kHz for a total of 600 samples, resolving 10 system flow through times. The additional sampling duration is required for the convergence of the unsteady RMS of observed flame oscillations.

4. Results

4.1. Shadowgraph

The shadowgraph light field has a baseline intensity $I_0(r, z)$ and experimental images $I(r, z)$ are biased by the flame. This bias is proportional to perturbations in the third-order spatial gradients in refractive index [56]. Because the index of refraction n is proportional to the fluid density ρ , the shadowgraph intensity bias is estimated by:

$$I - I_0 \propto \frac{d^3 n}{dz^3} \propto \frac{d^3 \rho}{dz^3} \quad (22)$$

This representation neglects density gradients in the radial direction; no significant radial gradients were observed in experiments or simulations.

In order to assess higher-dimensional effects in the OFB, flame thickness was resolved both spatially and temporally using shadowgraph images. For each time step t , at each radial location $r < 8$ mm, the following steps were used to compute a matrix of flame thickness values $\ell(r, t)$. First, the loop variables $r = R$ and $t = \tau$ were set and the one-dimensional profile of shadowgraph intensity values $I(R, z, \tau)$ is extracted. Both the position of the fuel surface $z_{\text{surf}}(R, \tau)$ and the position of the flame boundary $z_{\text{flame}}(R, \tau)$ were observed to correspond with prominent local minima in $I(R, z, \tau)$. The location of the most

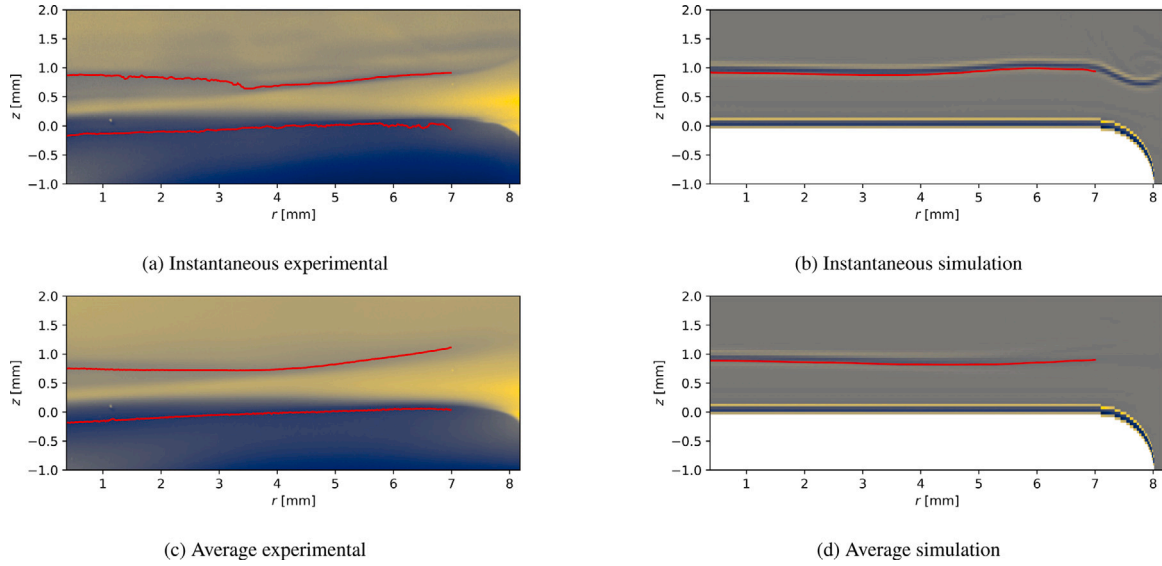


Fig. 5. Normalized shadowgraph intensity along fuel grain (false color), detected flame thickness and fuel surface super-imposed in red. (For interpretation of the references to color in this figure legend, the reader is referred to the web version of this article.)

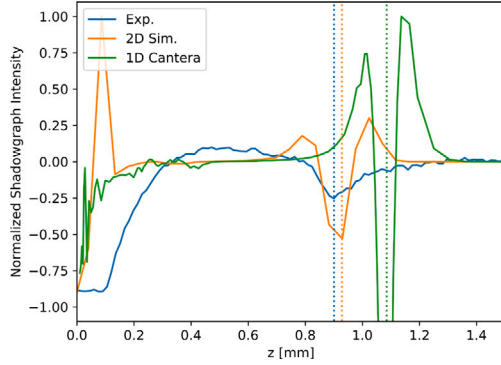


Fig. 6. Comparison of average normalized centerline shadowgraph intensity. Representative instantaneous experimental centerline shadowgraph intensity plotted for clarity. Dotted line is average computed flame thickness.

prominent local minimum within $-0.5 \text{ mm} < z < 0.1 \text{ mm}$ was chosen as $z_{\text{surf}}(R, \tau)$. (The $z = 0$ datum is based on a pre-combustion location of the fuel surface. During combustion, the local fuel surface position varied in r and t within these bounds.) The location of the most prominent local minimum within $0.3 \text{ mm} < z < 2.2 \text{ mm}$ was chosen as $z_{\text{flame}}(R, \tau)$. The flame thickness was obtained as the difference: $\ell(R, \tau) = z_{\text{flame}}(R, \tau) - z_{\text{surf}}(R, \tau)$.

The simulated shadowgraph intensity was estimated using a second-order finite difference approximation to estimate the third-order spatial derivatives. Fig. 5 shows instantaneous and average normalized shadowgraph intensity along the fuel grain surface for the experiment and numerical simulations, with the locations of z_{surf} and z_{flame} superimposed in red. In the experimental images, the flame thickness decreases along the radial axis up to around $r = 5 \text{ mm}$, followed by an increase as the fuel approaches the grain edge. This trend can also be seen in the simulated shadowgraph images, where there is the characteristic dip in shadowgraph intensity up to around $r = 5 \text{ mm}$, followed by an increase towards the edge of the fuel grain. Deviations from the average flame thickness highlight the oscillatory behavior of the flame observed in both experiments and simulations.

Fig. 6 shows a comparison of the average centerline shadowgraph intensity between experiment, quasi-one-dimensional simulation, and

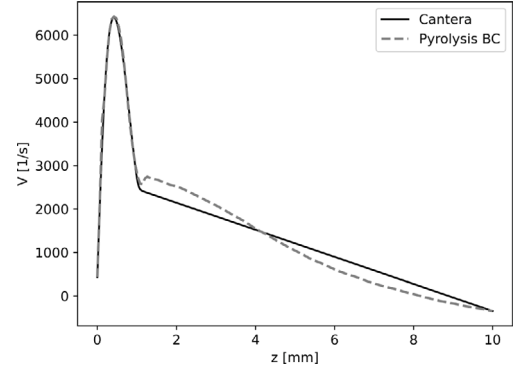


Fig. 7. Discrepancy of self-similarity profile with matching boundary conditions between quasi-one-dimensional model and LES.

two-dimensional axisymmetric LES simulation. The simulated shadowgraph intensity is normalized by the maximum intensity and the computed flame thickness is denoted by the corresponding dotted lines. Smoothing of the shadowgraph intensity between the experimental and numerical profiles is largely attributed to line-of-sight effects in experiments. Excellent qualitative agreement in the magnitude of flame thickness between the two-dimensional simulations and experiment highlight the efficacy of this model.

The quasi-one-dimensional flame significantly over-predicts the minimum in shadowgraph intensity, correlating to a significant over-prediction in the magnitude of flame thickness. To investigate, the exact boundary conditions from the pyrolysis boundary condition LES are specified in CANTERA and simulated using the Counterflow Diffusion Flame (CDF) solver [35]. Fig. 7 shows a comparison between the self-similarity profile, V , extracted from JENRE using:

$$V = -\frac{\partial(\rho v)}{\partial z} \cdot \frac{1}{2\rho} \quad (23)$$

and compared directly with quasi-one-dimensional results. With identical boundary conditions, there is significant deviation from self-similarity observed in the two-dimensional LES. The discrepancy affirms that the quasi-one-dimensional formulation is insufficient in capturing the complexities inherent to the OFB configuration. This can be partly attributed to the LES using a compressible formulation, with

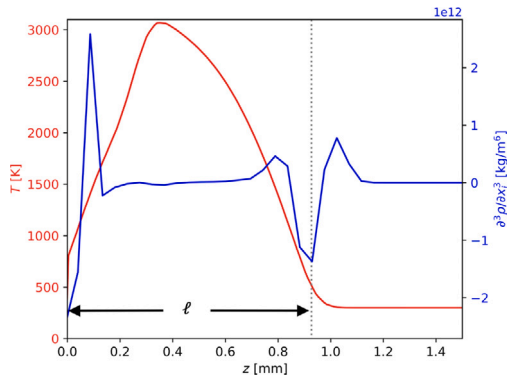


Fig. 8. Representative average simulated temperature and shadowgraph intensity above fuel surface, $r = 7$ mm. Annotated flame thickness using temperature threshold and shadowgraph intensity shown.

Table 5

Summary of average flame thickness [mm] comparison.

	Exp.	Pyrolysis BC	Constant inflow BC	1D Sim.
$\mu(\ell)$ [mm]	0.844	0.850	0.768	1.030
Percent error	–	0.71%	–9.01%	22.04%

non-constant pressure observed across the stagnation plane and flame.

4.2. Flame thickness and regression

A representative average at $r = 7$ mm of the simulated temperature and shadowgraph intensity are plotted together in Fig. 8. The dotted line shows the calculated flame thickness based on the minimum of shadowgraph intensity. The flame temperature, a primitive variable quantified directly in the LES formulation, has finer resolution in comparison to the derived simulated shadowgraph intensity. Therefore, a surrogate flame thickness is introduced using a temperature threshold in order to more robustly and accurately measure the temporally resolved flame thickness. The surrogate flame thickness, also denoted ℓ , is defined as the distance between the solid fuel surface and the location where $T = 500$ K on the oxidizer side of the established diffusion flame. This surrogate flame thickness was found to correspond directly, with high accuracy, to the average flame thickness calculated using shadowgraph intensity and is used for the remainder of this work.

Fig. 9 shows the average flame thickness, $\mu(\ell)$, and standard deviation of flame thickness, $\sigma(\ell)$, for the experimental and simulated flames. Experimental imaging shows that the mean flame thickness decreases slightly with increasing radial location to a local minimum at $r = 4$ mm, and subsequently increases moving out across the fuel grain. The axisymmetric LES simulations, both with the constant inflow and pyrolysis boundary conditions, are able to replicate this trend in flame thickness with a local minimum in flame thickness occurring at roughly $r = 4.5$ mm for the pyrolysis boundary condition. The average flame thickness across the fuel grain is given in Table 5. The magnitude of flame thickness predicted by the pyrolysis, $\mu(\ell) = 0.850$ mm, and constant inflow BC, $\mu(\ell) = 0.768$ mm, axisymmetric LES simulations shows good agreement with the experimental magnitude, $\mu(\ell) = 0.844$ mm. The improvement is drastic over the quasi-one-dimensional modeling, $\mu(\ell) = 1.030$ mm, which significantly overpredicts the magnitude of flame thickness. The magnitude of predicted flame thickness using the pyrolysis boundary condition is within less than 1% of the experimental magnitude, demonstrating excellent agreement. The constant inflow boundary condition, with the same mass flow rate as the quasi-one-dimensional model, shows improved flame thickness prediction over the quasi-one-dimensional model, further indicating self-similarity is not satisfied by the OFB configuration.

The experimental flame thickness shows a weak trend of increasing standard deviation across the fuel grain, with a large standard deviation seen near the fuel centerline. This large centerline standard deviation can be partly attributed to line of sight measurement uncertainty which are highest near the flame centerline. The axisymmetric simulations show a monotonic increase in the standard deviation of flame thickness across the fuel grain surface, with a magnitude less than experiment. Without the line of sight measurement and fuel surface uncertainty, the flame thickness can be measured directly in the numerical simulations, manifesting in a standard deviation that directly reflects the magnitude of local flame oscillations. Across the fuel surface, the magnitude of flame oscillation increases monotonically due to the influence of vortex shedding in the nozzle shear layer. The experimental standard deviation of flame thickness includes both the influence of flame oscillation and measurement uncertainty, indicating a similar level of flame oscillation with the highest oscillations seen along the fuel grain edge. The standard deviation increases in magnitude with the pyrolysis boundary as compared to the constant inflow boundary condition, suggesting that the variation in blowing velocity as a consequence of time-dependent regression rate results in larger flame oscillations.

To further investigate the unsteady OFB flame oscillations, the temporal history of the flame thickness is sampled at $r = 7$ mm and a power spectral density (PSD) was calculated using a FFT of the time history. Fig. 10 displays the temporal history of flame thickness and corresponding PSD for experimental and simulated flame thickness. The time history demonstrates good qualitative agreement between the experimental and numerical flames in capturing the oscillatory nature of the OFB flame. The experimental flame thickness at $r = 7$ mm shows larger magnitudes in the fluctuations as compared to the numerical simulations. The PSD of the experimental flame thickness shows a broad peak in spectral intensity between 2.5 and 5 kHz, with a flattening of the intensity beyond 10 kHz which suggests high-frequency experimental noise. The numerical simulations show good trend-wise agreement with the experimental PSD up to around 7.5 kHz, with broad peaks also centered around 2.5 and 5 kHz. There is excellent agreement between the PSD signatures of the simulations with the pyrolysis and constant inflow boundary conditions. This suggests that the flame dynamics are not driven by pyrolysis, but are largely driven by the unsteady fluid dynamics.

One of the main utilities of OFB configuration is to quickly characterize the regression rate of different solid fuels. Fig. 11 shows a comparison between the regression rate prediction of the experiment, axisymmetric simulation, and quasi-one-dimensional model. In experiments, the bulk regression rate is determined by the position history of the burner's stepper motor (see Fig. 1) and the regression rate data is not resolved in radius [36]. Numerical simulations show variation of regression rate across the fuel surface consistent with the variation in flame thickness observed. As the flame thickness reaches a minimum at $r = 5$ mm, the simulated regression rate reaches a maximum. This inverse relationship is driven by the higher heat flux into the fuel surface as the flame is positioned closer to the fuel surface. Table 6 summarizes the average regression rate comparisons between the experiment, axisymmetric simulation, and quasi-one-dimensional model. Contrary to the prediction of flame thickness, there is not major improvement in the prediction of regression rate magnitude, with the axisymmetric simulations overpredicting the magnitude of regression by 24.4% as compared to the quasi-one-dimensional simulations underpredicting the regression rate magnitude 15.5%. The overprediction of regression rate in LES is attributed to the improved prediction of flame standoff increasing the thermal gradients near the fuel surface and prediction of peak temperature close to the adiabatic flame temperature. Flame imaging of the OFB shows large amounts of soot [18], not included in the chemistry mechanism formulation, that inhibit the maximum flame temperature and resulting heat flux at the fuel surface. Of note, the profile of regression rate is considered idealized, as this work does

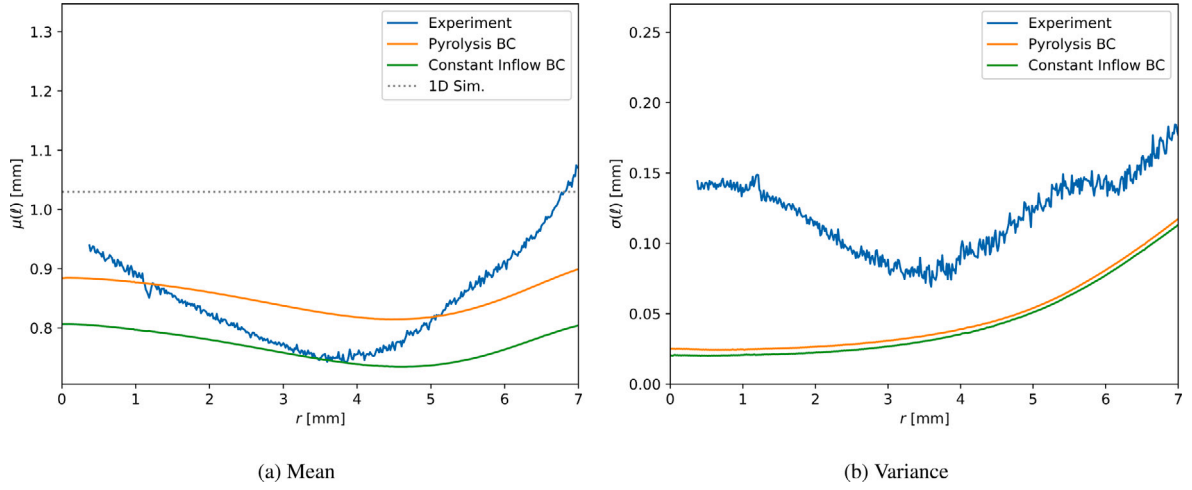


Fig. 9. Comparison of flame thickness prediction.

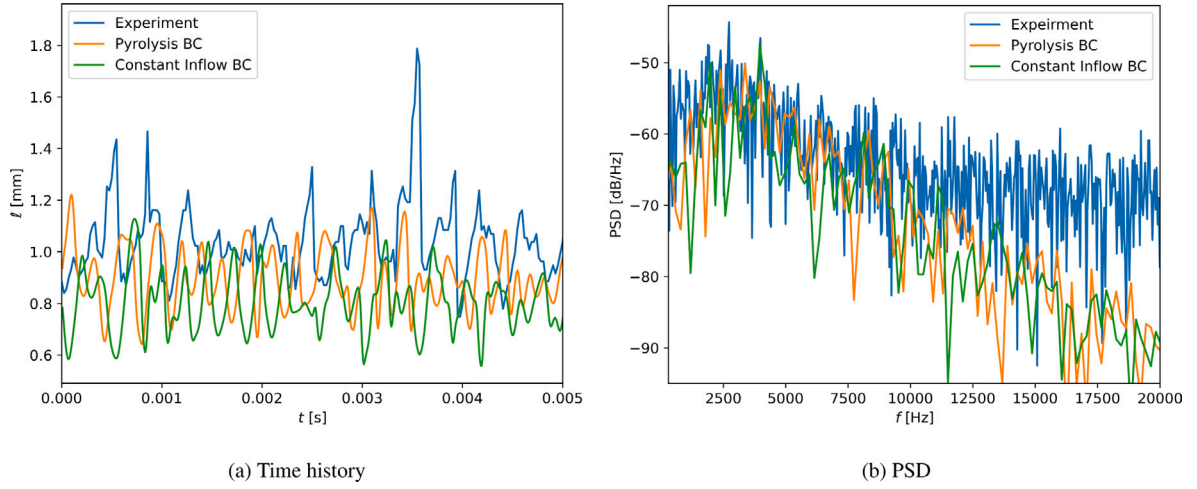
Fig. 10. Temporal evolution of flame thickness at $r = 7$ mm.

Table 6

Summary of average regression rate comparison.

	Exp.	Pyrolysis BC	1D Sim.
Magnitude	0.46	0.588	0.394
Percent error	—	24.4%	−15.5%

not consider variations to the fuel surface topography. Experimental imaging, alongside inspection of burned fuel grains, does not show evidence of any significant fuel surface concavity. This suggests that the fuel surface topography is largely self-correcting through variation in the regression rate. As small surface deformations develop, local surface peaks will protrude further into the flow-field closer to the stagnation plane resulting in both larger thermal and velocity gradients. This results in higher heat transfer and regression rate at these surface peaks, flattening out local peaks and self-correcting the surface topography.

The intimate connection between the average flame thickness and regression rate across the fuel grain surface indicates the two quantities are dynamically coupled. To visualize this, a time history of flame thickness and regression rate are sampled at $r = 7$ mm and normalized. The normalized flame thickness, $\tilde{\ell}$, and normalized regression rate, \tilde{z} , are defined as:

$$\tilde{\ell} = \frac{1 - (\dot{\ell} - \mu(\ell))}{\ell_{\max}} \quad (24)$$

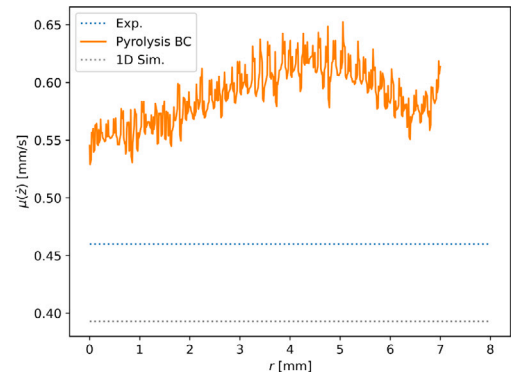


Fig. 11. Comparison of regression rate prediction.

$$\tilde{z} = \frac{\dot{z} - \mu(\dot{z})}{\dot{z}_{\max}} \quad (25)$$

where the normalized flame thickness is inverted for easier visualization. Fig. 12 plots the time history comparison between the normalized flame thickness and regression rate at $r = 7$ mm. It is immediately clear that the two quantities are indeed dynamically coupled through time. The pyrolysis boundary condition employed in this work assumes that

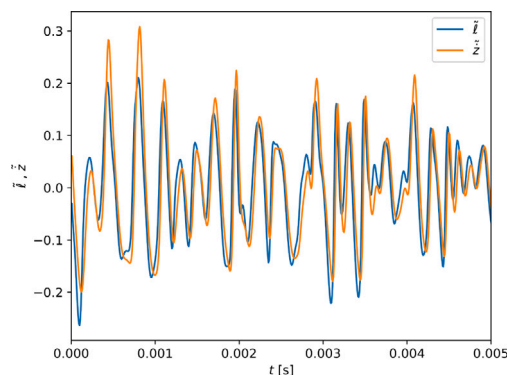


Fig. 12. Coupling between instantaneous normalized flame thickness and regression rate.

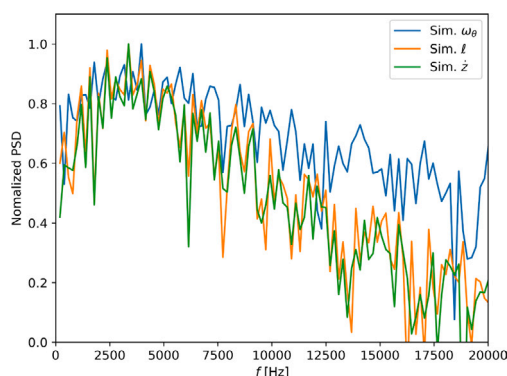


Fig. 13. Normalized PSD comparison between flame thickness, regression rate, and vorticity.

the fuel grain has no thermal mass and is always in thermal equilibrium with the fuel surface. This results in no phase lag between the simulated flame thickness and pyrolysis as the fuel surface (and subsequently the fuel grain) can instantaneously adjust to the imposed flame gradient. If this assumption at the surface is relaxed, it is hypothesized that a phase lag between the regression rate and flame thickness would develop, as the fuel surface temperature would be lagged by the thermal mass of the fuel grain. For this work, the variation in fuel surface temperature is minimal, with a maximum of 15 K difference at $r = 7$ mm, however, the phase lag could be important for capturing coupled dynamics in SFRJ and HRE engines which contain much greater variance of regression rate and fuel temperatures along the fuel surface [2,19].

Excellent agreement between the PSD response of the pyrolysis and constant inflow simulation flame thickness (as was shown in Fig. 10(b)) suggest that the flame dynamics are driven by the unsteady fluid dynamics. To investigate this, Fig. 13 shows the normalized PSD spectra for the flame thickness and regression rate at $r = 7$ mm, as well as the azimuthal vorticity, ω_θ , sampled upstream at 4 mm above the grain at the center of nozzle lip width, $r = 4.4$ mm. The azimuthal vorticity corresponds directly with the intermittent vortex shedding from the nozzle lip, serving as a marker for the unsteady fluid dynamics. The PSD spectra of the flame thickness and regression rate show excellent agreement confirming the above-mentioned coupling. The PSD spectra of the flame thickness and azimuthal vorticity show excellent agreement for frequencies below 5 kHz, but begin to diverge beyond this point. The agreement below 5 kHz suggests that the vortex shedding is indeed driving the unsteady flame oscillations, which are subsequently driving the regression rate. Similarly, spectral-proper orthogonal decomposition of optically accessible SFRJ engine flowfields has demonstrated

that the coupled flow-flame interaction is largely dominated by the low-frequency vortex shedding generated at the backward-facing step of the combustor [3]. Seminal studies [57] on the response of non-premixed counterflow flames subject to periodic perturbations demonstrate that at low frequencies the flame is able to respond instantaneously in phase. However, at higher frequencies there is a significant phase delay and the magnitudes of perturbations are diminished. The PSD analysis suggests a similar trend in which the low frequency periodic vortex shedding is driving and coupled with the flame dynamics observed. The higher frequency unsteady fluid dynamic content is not able to couple with the combustion dynamics. Subsequently, the gas-phase combustion dynamics largely drive the dynamic response in the fuel grain regression rate. As mentioned above, the variation in blowing velocity as a result of variations in regression rate results in larger flame oscillations providing bi-directional coupling between the flame dynamics and regression rate dynamics.

4.3. 2D flame structure

Validation of the simulated results with experimental shadowgraph, flame thickness, and regression rate, indicate that two-dimensional axisymmetric LES simulations are a suitable tool for exploring the combustion physics in the OFB geometry. Fig. 14 displays the instantaneous temperature, azimuthal vorticity, Y_{CO} , and Y_{CO_2} of the simulation with coupled pyrolysis boundary condition to visualize higher-dimensional aspects of the OFB combustion dynamics. The instantaneous flame markers elucidate the unsteady nature of the OFB combustion dynamics in which azimuthal vorticity contours display regular vortex shedding from the nozzle lip, advected downstream towards the fuel grain lip. The temperature, Y_{CO} , and Y_{CO_2} contours capture flame roll-up and wrinkling as a consequence of the interactions with the vorticity. Most of the larger flame roll-up occurs downstream of the fuel grain, $r > 8$ mm, resulting in smaller perturbations to the flame thickness above the fuel grain surface. In corroboration with previous normalized PSD results, this suggests that the main driver of the unsteady combustion and regression dynamics is the vortex shedding from the nozzle lip.

The Y_{CO} and Y_{CO_2} shows evidence of a bifurcated secondary diffusion front and incomplete combustion along the fuel grain surface. The CO to CO₂ oxidation is not complete until significantly downstream from the fuel grain, $r > 15$ mm. There is some evidence of ambient entrainment below the flame creating a bifurcated secondary diffusion front. The flame shape curves slightly down past the fuel grain edge, consistent with experimentally imaged flames with $\dot{m}''_{ox} > 8$ kg/(m²s) [18]. Although the downstream portion of the flame has a little direct effect on the solid fuel regression rate, the flame dynamics reaching out above $r > 20$ mm have significant effects on the line of sight measurement and experimental uncertainty. Large oscillations of the flame above the solid fuel grain surface, $r > 5$ mm, adds to uncertainty in all line of sight techniques. This has particularly large effect when imaging the flame at $r = 0$ mm, where the line of sight is maximally influenced by the downstream combustion dynamics.

Fig. 15 displays the average temperature, azimuthal vorticity, Y_{CO} , and Y_{CO_2} of the simulation with coupled pyrolysis boundary condition. The average contours confirms the secondary diffusion flame structure and the supply of vorticity from the nozzle. The average azimuthal vorticity contour also highlights the vorticity production from the shear layer formed along the fuel grain surface. With increasing radius, there is a larger magnitude of vorticity along the fuel grain surface and in the flame region due to the proximity of the fuel grain surface with the stagnation plane. This is directly linked to an increase in radial velocity required by conservation of mass at the stagnation point, resulting in boundary layer development, accompanied by vorticity generation, along the fuel grain surface.

The balance of convective and diffusive transport along the fuel grain manifests in a radial dependence of average surface composition. Eqs. (18)–(20) solve for the diffusion and collection of species to the

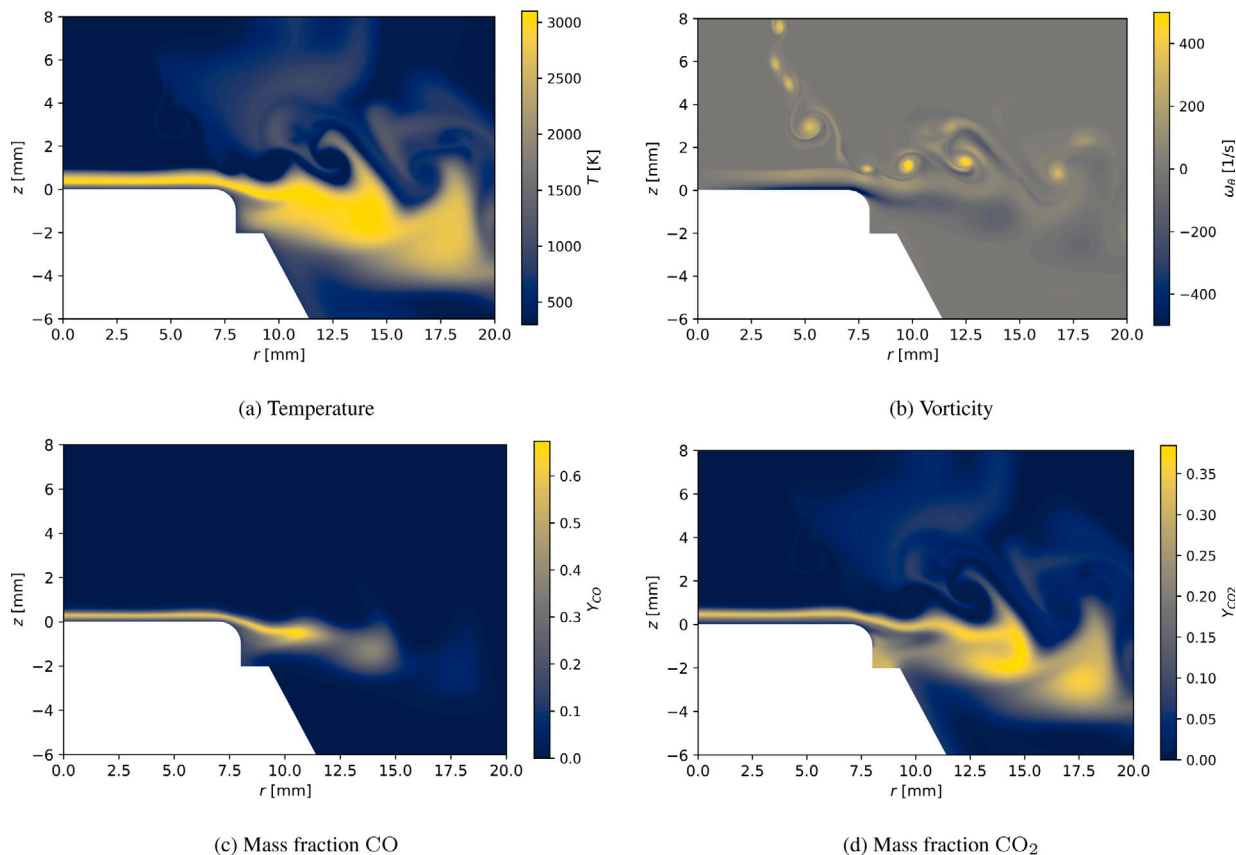


Fig. 14. Instantaneous simulated flame-marking contours.

fuel surface as a result of close flame proximity. Products from the flame are also convected in the radially outward direction, changing the composition above the fuel grain surface and subsequently influencing the species surface deposition. Fig. 16 shows the radial dependence of average surface mass fractions for representative major and minor species normalized for readability. Table 7 displays the average surface mass fractions of the first seven species with the largest surface mass fraction for reference. Along the fuel grain surface, there is a significant radial dependence of major species CO, CO₂, and H₂O. Due to convection of upstream products, the surface deposition of CO₂ and H₂O increase by approximately 3% and 2%, respectively, from the centerline to radius $r = 7$ mm. Likewise, there is a decrease of CO by approximately 2% across the fuel grain surface. The variation in composition further highlights the inadequacy of the quasi-one-dimensional formulation in modeling the OFB, in which a constant fuel composition is assumed. Due to the proximity of the stagnation plane to the fuel surface, the upstream combustion products are advected radially and deposited at the fuel surface through diffusion.

The composition of minor species at the surface further highlight the intricacy of modeling the OFB, in which there are more pronounced variations of surface composition >20% and >50% for minor species O₂ and OH at the surface. The variation in both O₂ and OH follow directly in the variation with flame thickness and regression. As the fuel surface temperature and temperature gradients change along the fuel grain surface the composition of radicals can have large variation. Further, the variations in flame thickness results in more or less diffusion of oxygen to the fuel surface, allowing for faster radical generation. This introduces further complexity in the coupling between flame dynamics with both overall fuel regression rate and local surface composition.

Table 7

Average surface mass fraction.

$Y_{C_2H_6}$	Y_{CO}	$Y_{C_2H_2}$	Y_{H_2O}	Y_{CO_2}	Y_{CH_3CO}	Y_{H_2}
0.7129	0.1208	0.0523	0.0339	0.0335	0.0110	0.0061

5. Conclusion

This work describes an experimental and numerical comparison of temporally resolved combustion dynamics of an HTPB opposed flow burner (OFB) configuration. Failure of the OFB to meet self-similarity requirements of quasi-one-dimensional modeling resulted in the need for modeling with higher fidelity, using a two-dimensional LES approach. Time-resolved simulations with and without a fully-coupled gas-solid pyrolysis boundary condition are performed to compare shadowgraph intensity, flame thickness, and regression rate with experimental prediction. The two-dimensional simulations show marked improvement in the prediction of flame thickness over quasi-one-dimensional modeling with respect to experiment.

Additional spatial and temporal resolution provided by two-dimensional LES simulations provided a means for exploring the higher-dimensional structural and unsteady flame dynamics of the OFB. The average flame thickness shows a decrease in magnitude with increasing radius up to $r \approx 5$ mm, followed by an increase in magnitude with additional radial distance. PSD of the flame thickness shows good agreement to experiment in the broad peak frequency seen in the flame oscillations. The numerical simulations show a strong coupling of the instantaneous regression rate and flame thickness, that appear to be driven by the low-frequency vortex-shedding from the OFB nozzle

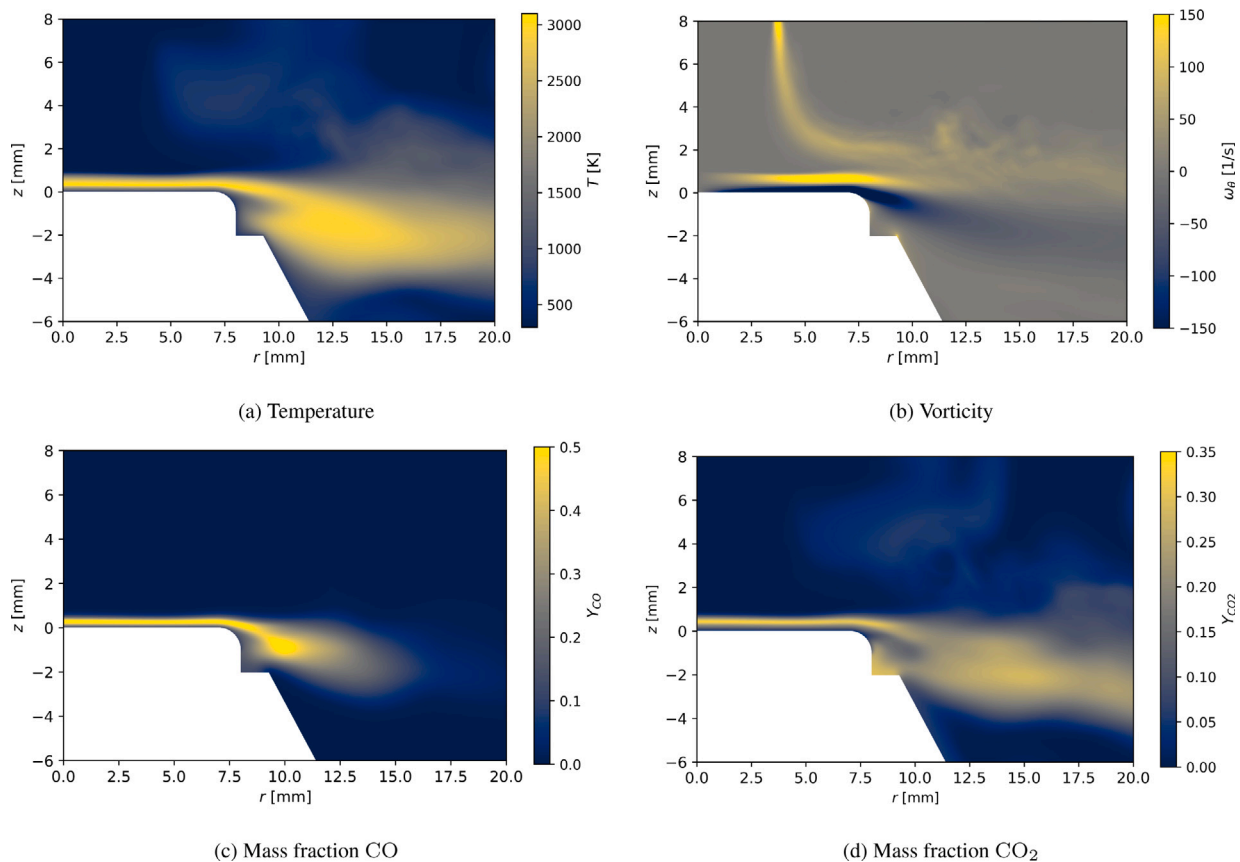


Fig. 15. Average simulated flame-marking contours.

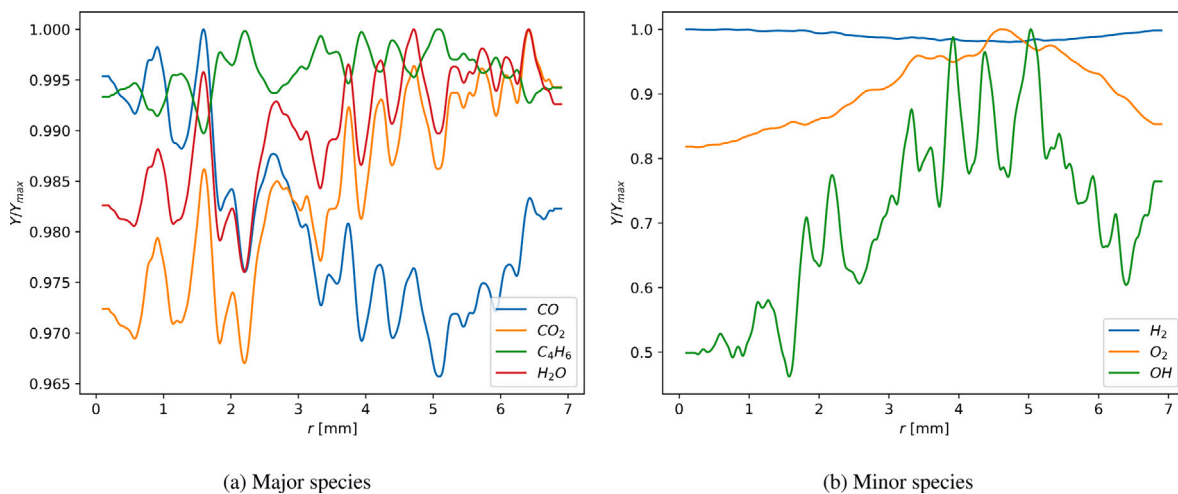


Fig. 16. Radial dependence of average surface mass fractions of representative species.

lip. Additional analysis of the two-dimensional simulations showed the competition between diffusive and convective transport along the proximal stagnation plane leads to variation in species composition across the fuel grain surface. The majority of the CO to CO₂ oxidation is relegated to downstream of the fuel grain, where ambient entrainment leads to a double diffusion flame.

In future work, resolution of the boundary layer development within the nozzle and particle-image velocimetry (PIV) will be employed to study the effect on flame dynamics and further assess the quasi-one-dimensional self-similarity. Extension to three-dimensional modeling is

necessary to capture the turbulent flame dynamics with the inclusion of radiation, particles, and soot, valuable to characterizing the OFB system and exploring the coupled physics. Additional experimental diagnostics could also improve comparison with simulations. Planar laser-induced fluorescence (PLIF) imaging could produce species concentration maps that could be compared directly to simulation outputs such as Y_{OH} or Y_{CH_2O} . Experimental temperature measurements could also be obtained through pyrometry or emission spectroscopy of hydrocarbon intermediate species such as CH and C₂ to improve modeling and understanding of solid fuel combustion.

CRedit authorship contribution statement

Ryan DeBoskey: Writing – review & editing, Writing – original draft, Visualization, Software, Methodology, Investigation, Formal analysis, Data curation, Conceptualization. **Clayton Geipel:** Writing – review & editing, Writing – original draft, Methodology, Investigation, Formal analysis, Data curation. **David Kessler:** Writing – review & editing, Supervision, Methodology, Investigation, Funding acquisition, Conceptualization. **Brian Bojko:** Writing – review & editing, Supervision, Formal analysis, Conceptualization. **Brian Fisher:** Supervision, Methodology, Investigation, Funding acquisition. **Ryan F. Johnson:** Writing – review & editing, Validation, Supervision, Software, Investigation. **Venkat Narayanaswamy:** Writing – review & editing, Supervision, Conceptualization.

Declaration of competing interest

The authors declare that they have no known competing financial interests or personal relationships that could have appeared to influence the work reported in this paper.

Acknowledgments

This work was sponsored by the Office of Naval Research, United States through the NRL 6.1 Base Program and the Hypersonic Aerothermodynamics, High-Speed Propulsion and Materials portfolio (PM: Dr. Eric Marineau). The authors would like to acknowledge Drs. Andrew Kercher, Andrew Corrigan, and Eric Ching for assistance provided with the overall computational framework of the JENRE[®] Multiphysics Framework, and Drs. Albert Epshteyn and Matthew Finn for producing the HTPB fuel strands. Ryan DeBoskey was supported by DoD NDSEG Fellowship.

Appendix A. Supplementary data

Supplementary material related to this article can be found online at <https://doi.org/10.1016/j.combustflame.2024.113960>. Instantaneous videos of experimental shadowgraph and calculated experimental flame thickness (Experimental_Flamethickness.mp4), simulated temperature (Numerical_Temperature.mp4), and simulated vorticity (Numerical_Vorticity.mp4) are provided with corresponding flame thickness and fuel surface marked.

References

- [1] A. Ajaz, Hydroxyl-terminated polybutadiene telechelic polymer (HTPB): binder for solid rocket propellants, *Rubber Chem. Technol.* 68 (3) (1995) 481–506.
- [2] S. Krishnan, P. George, Solid fuel ramjet combustor design, *Prog. Aerosp. Sci.* 34 (1998) 219–256.
- [3] W.C. Senior, R.M. Gejji, C.D. Slabaugh, Flame dynamics in an optically accessible solid fuel ramjet combustor, *J. Propul. Power* (2023) 1–10.
- [4] H. Zhang, N. Wang, Z. Wu, G. Fang, Z. Wei, Preliminary investigation of paraffin-based fuel combustion in solid fuel scramjet, *Acta Astronaut.* 173 (2020) 119–130.
- [5] N. Davydenko, R. Gollender, A. Gubertov, V. Mironov, N. Volkov, Hybrid rocket engines: The benefits and prospects, *Aerosp. Sci. Technol.* 11 (1) (2007) 55–60.
- [6] C. Dennis, B. Bojko, On the combustion of heterogeneous AP/HTPB composite propellants: A review, *Fuel* 254 (2019) <http://dx.doi.org/10.1016/j.fuel.2019.115646>.
- [7] G. Schulte, Fuel regression and flame stabilization studies of solid-fuel ramjets, *J. Propul. Power* 2 (1986) 301–304.
- [8] W.S. Blazowski, An Investigation of the Combustion Characteristics of Some Polymers Using the Diffusion-Flame Technique (Ph.D. thesis), Stevens Institute of Technology, 1971.
- [9] K. Seshadri, F.A. Williams, Structure and extinction of counterflow diffusion flames above condensed fuels: Comparison between poly(methyl methacrylate) and its liquid monomer, both burning in nitrogen–air mixtures, *J. Polym. Sci. Polym. Chem. Ed.* 16 (7) (1978) 1755–1778.
- [10] D. Holve, R. Sawyer, Diffusion controlled combustion of polymers, *Symp. (Int.) Combust.* 15 (1) (1975) 351–361, 15 *Symp. (Int.) Combust.*.
- [11] G. Risha, G. Harting, K. Kuo, A. Peretz, D. Koch, H. Jones, J. Arves, Pyrolysis and combustion of solid fuels in various oxidizing environments, in: 34th AIAA/ASME/SAE/ASEE Joint Propulsion Conference and Exhibit, 1998, p. 3184.
- [12] G. Young, G. Risha, A. Miller, R. Glass, T. Connell, R. Yetter, Combustion of alane-based solid fuels, *Int. J. Energ. Mater. Chem. Propuls.* 9 (3) (2010) 249–266.
- [13] G. Young, C.A. Stoltz, B.P. Mason, V.S. Joshi, R.H. Johansson, T.L. Connell Jr., G. Risha, R.A. Yetter, Combustion of PTFE-Boron compositions for propulsion applications, *Int. J. Energ. Mater. Chem. Propuls.* 11 (2012) 451–471.
- [14] G. Young, J.J. Koeck, N.T. Conlin, J.L. Sell, G.A. Risha, Influence of an electric field on the burning behavior of solid fuels and propellants, *Propell. Explos. Pyrot.* 37 (1) (2012) 122–130.
- [15] G. Young, C. Roberts, S. Dunham, Combustion behavior of solid oxidizer/gaseous fuel diffusion flames, *J. Propul. Power* 29 (2) (2013) 362–370.
- [16] S. Shark, C. Zaseck, T. Pourpoint, S. Son, Solid-fuel regression rates and flame characteristics in an opposed flow burner, *J. Propul. Power* 30 (6) (2014) 1675–1682.
- [17] G. Young, G.A. Risha, T.L. Connell Jr., R.A. Yetter, Combustion of HTPB based solid fuels containing metals and metal hydrides with nitrous oxide, *Propell. Explos. Pyrot.* 44 (6) (2019) 744–750.
- [18] C.M. Geipel, B.T. Bojko, C.J. Pfützner, B.T. Fisher, R.F. Johnson, Regression of solid polymer fuel strands in opposed-flow combustion with gaseous oxidizer, *Proc. Combust. Inst.* 39 (3) (2023) 3389–3399.
- [19] D. Gallegos, H. Pace, C. Arnold, L. Massa, G. Young, Regression and flame structure in cavity flameholding solid-fuel ramjet fuel grains, *J. Propul. Power* (2023) 1–11.
- [20] H. Pace, C. Arnold, D. Gallegos, G. Young, L. Massa, Acoustics in flameholding solid-fuel-ramjet fuel grains, *AIAA J.* 61 (10) (2023) 4579–4597.
- [21] L. Krishnamurthy, F. Williams, A flame sheet in the stagnation-point boundary layer of a condensed fuel, *Acta Astronaut.* 1 (5–6) (1974) 711–736.
- [22] J. T'ien, S. Singhal, D. Harrold, J. Pahl, Combustion and extinction in the stagnation-point boundary layer of a condensed fuel, *Combust. Flame* 33 (1978) 55–68.
- [23] J.L. Rhatigan, H. Bedir, S. James, Gas-phase radiative effects on the burning and extinction of a solid fuel, *Combust. Flame* 112 (1–2) (1998) 231–241.
- [24] G.A. Marxman, Boundary-layer combustion in propulsion, in: *Symp. (Int.) Combust.*, Vol. 11, No. 1, Elsevier, 1967, pp. 269–289.
- [25] J. Rolon, D. Veynante, J. Martin, F. Durst, Counter jet stagnation flows, *Exp. Fluids* 11 (5) (1991) 313–324.
- [26] J.M. Berghthorson, S.D. Salusbury, P.E. Dimotakis, Experiments and modelling of premixed laminar stagnation flame hydrodynamics, *J. Fluid Mech.* 681 (2011) 340–369.
- [27] J.M. Berghthorson, K. Sone, T.W. Mattner, P.E. Dimotakis, D.G. Goodwin, D.I. Meiron, Impinging laminar jets at moderate Reynolds numbers and separation distances, *Phys. Rev. E* 72 (6) (2005) <http://dx.doi.org/10.1103/PhysRevE.72.066307>.
- [28] B. Sarnacki, G. Esposito, R. Krauss, H. Chelliah, Extinction limits and associated uncertainties of nonpremixed counterflow flames of methane, ethylene, propylene and n-butane in air, *Combust. Flame* 159 (3) (2012) 1026–1043.
- [29] C. Frouzakis, J. Lee, A. Tomboulides, K. Boulouchos, Two-dimensional direct numerical simulation of opposed-jet hydrogen-air diffusion flame, in: *Symp. (Int.) Combust.*, 27, (1) Elsevier, 1998, pp. 571–577.
- [30] V. Mittal, H. Pitsch, F. Egolfopoulos, Assessment of counterflow to measure laminar burning velocities using direct numerical simulations, *Combust. Theor. Model.* 16 (3) (2012) 419–433.
- [31] N. Bouvet, D. Davidenko, C. Chauveau, L. Pillier, Y. Yoon, On the simulation of laminar strained flames in stagnation flows: 1D and 2D approaches versus experiments, *Combust. Flame* 161 (2) (2014) 438–452.
- [32] R. Johnson, A. VanDine, G. Esposito, H. Chelliah, On the axisymmetric counterflow flame simulations: Is there an optimal nozzle diameter and separation distance to apply quasi one-dimensional theory? *Combust. Sci. Technol.* 187 (1–2) (2015) 37–59.
- [33] A.E. Lutz, R.J. Kee, J.F. Grcar, F.M. Rupley, OPPDIF: A Fortran Program for Computing Opposed-Flow Diffusion Flames, Tech. rep, Sandia National Lab.(SNL-CA), Livermore, CA (United States), 1997.
- [34] M. Smooke, J. Crump, K. Seshadri, V. Giovangigli, Comparison between experimental measurements and numerical calculations of the structure of counterflow, diluted, methane-air, premixed flames, in: *Symp. (Int.) Combust.*, Vol. 23, No. 1, Elsevier, 1991, pp. 463–470.
- [35] D. Goodwin, An open-source, extensible software suite for CVD process simulation, *Chem. Vap. Deposition XVI EUROCDV* 14 (40) (2003) 2003–2008.
- [36] C.M. Geipel, C.J. Pfützner, B.T. Fisher, Active control of fuel position in opposed-flow strand burner experiments, *Combust. Sci. Technol.* 196 (9) (2024) 1267–1284.
- [37] B.J. McBride, S. Gordon, M.A. Reno, Coefficients for Calculating Thermodynamic and Transport Properties of Individual Species, Tech. Rep. NASA-TM-4513, NASA Glenn Research Center, Cleveland Ohio, 1993.
- [38] B.J. McBride, M.J. Zehe, S. Gordon, NASA Glenn Coefficients for Calculating Thermodynamic Properties of Individual Species, Tech. Rep. NASA/TP-2002-211556, NASA Glenn Research Center, Cleveland Ohio, 2002.

- [39] T. Coffee, J. Heimerl, Transport algorithms for premixed, laminar steady-state flames, *Combust. Flame* 43 (1981) 273–289.
- [40] R. Houim, K. Kuo, A low-dissipation and time-accurate method for compressible multi-component flow with variable specific heat ratios, *J. Comput. Phys.* 230 (23) (2011) 8527–8553.
- [41] R.J. Kee, J.A. Miller, G.H. Evans, G. Dixon-Lewis, A computational model of the structure and extinction of strained, opposed flow, premixed methane-air flames, *Symp. (International) Combust.* 22 (1) (1989) 1479–1494.
- [42] R.J. Kee, M.E. Coltrin, P. Glarborg, *Chemically Reacting Flow: Theory and Practice*, Wiley, Hoboken, NJ, 2005.
- [43] C. R. Wilke, A viscosity equation for gas mixtures, *J. Chem. Phys.* 18 (1950) 517–519.
- [44] S. Mathur, P.K. Tondon, S.C. Saxena, Thermal conductivity of binary, ternary and quaternary mixtures of rare gases, *Mol. Phys.* 12 (1967) 569–579.
- [45] R. Hartmann, P. Houston, An optimal order interior penalty discontinuous Galerkin discretization of the compressible Navier-Stokes equations, *J. Comput. Phys.* 227 (2008) 9670–9685.
- [46] D.I. Ketcheson, Highly efficient strong stability-preserving Runge–Kutta methods with low-storage implementations, *SIAM J. Sci. Comput.* 30 (4) (2008) 2113–2136.
- [47] R.F. Johnson, A.D. Kercher, A conservative discontinuous Galerkin discretization for the chemically reacting Navier-Stokes equations, *J. Comput. Phys.* 423 (2020) <http://dx.doi.org/10.1016/j.jcp.2020.109826>.
- [48] F. Bassi, F. Cecchi, N. Franchina, S. Rebay, M. Savini, High-order discontinuous Galerkin computation of axisymmetric transonic flows in safety relief valves, *Comput. & Fluids* 49 (1) (2011) 203–213.
- [49] R.D. DeBoskey, D.A. Kessler, B.T. Bojko, R.F. Johnson, G.B. Goodwin, The influence of chemical reaction models on combustion dynamics in an opposed-flow solid fuel burner, in: *AIAA SCITECH 2023 Forum*, 2023, p. 0161.
- [50] H. Arisawa, T. Brill, Flash pyrolysis of hydroxyl-terminated polybutadiene (HTPB) I: Analysis and implications of the gaseous products, *Combust. Flame* 106 (1–2) (1996) 131–143.
- [51] H. Arisawa, T. Brill, Flash pyrolysis of hydroxyl-terminated polybutadiene (HTPB) II: Implications of the kinetics to combustion of organic polymers, *Combust. Flame* 106 (1–2) (1996) 144–154.
- [52] D. Bianchi, B. Betti, F. Nasuti, C. Carmicino, Simulation of gaseous oxygen/hydroxyl-terminated polybutadiene hybrid rocket flowfields and comparison with experiments, *J. Propul. Power* 31 (3) (2015) 919–929.
- [53] A. Laskin, H. Wang, C.K. Law, Detailed kinetic modeling of 1,3-butadiene oxidation at high temperatures, *Int. J. Chem. Kinet.* 32 (10) (2000) 589–614.
- [54] P. Ciotolli, M. Galassi, P. Lapenna, G. Leccese, D. Bianchi, F. Nasuti, F. Creta, M. Valorani, CSP-based chemical kinetics mechanisms simplification strategy for non-premixed combustion: An application to hybrid rocket propulsion, *Combust. Flame* 186 (2017) 83–93.
- [55] H.J. Curran, P. Gaffuri, W.J. Pitz, C.K. Westbrook, A comprehensive modeling study of n-heptane oxidation, *Combust. Flame* 114 (1998) 149–177.
- [56] W. Bachalo, *Methods for compressible flows*, in: A. Smits, T. Lin (Eds.), *Flow Visualization: Techniques and Examples*, second ed., Imperial College Press, London, 2012, pp. 236–237.
- [57] F.N. Egolfopoulos, C.S. Campbell, Unsteady counterflowing strained diffusion flames: diffusion-limited frequency response, *J. Fluid Mech.* 318 (1996) 1–29.